CrossMark

Development of Self-Assembled Titania Nanopore Arrays for Orthopedic Applications

K. Indira[1,2] · U. Kamachi Mudali[3] · N. Rajendran[1]

Abstract Self-assembled TiO_2 nanopore arrays (TNPA) were developed by electrochemical anodization. Microscopic studies revealed the presence of nanoporous surface with pore diameter and length of about 84 and 100 nm, respectively. Growth of apatite (HAp) on TNPA after immersion in Hank's solution for different durations such as 3, 5, and 7 days was confirmed by various spectroscopic studies. Polarization study exhibited that the specimens after immersion in Hank's solution showed high corrosion resistance which is attributed to the HAp growth on TNPA surface. Hence, TNPA is a viable material with required biocompatibility and corrosion resistance for use as orthopedic implants.

Keywords Anodization · Nanopore arrays · Apatite · Corrosion resistance · Orthopedic implant

1 Introduction

Recent research focuses on the development of bioactive materials such as metals and their alloys, which are extensively used in implant applications. Such an implant materials exhibit high strength and toughness. However, they are susceptible to chemical and electrochemical degradation, which leads to corrosion [1]. The main objectives in the design of next generation dental and orthopedic implants are enhancement of biocompatibility and corrosion resistance [2].

In this context, titanium (Ti) and its alloys stand first for implant materials due to their biocompatibility with human bone and blood [3–6]. They have many desirable properties such as relatively low modulus (similar to human bone), good fatigue strength [7–9]. In addition, they have excellent corrosion resistance which is due to native oxide layer present on their surface [10–12]. However, the oxide layer is bio-inert which leads to insufficient new bone formation on Ti surface, subsequently implant loosening and failure [13, 14]. Besides, the patient needs to undergo a painful revision surgery. Therefore, to overcome these complications, the surface of Ti needs to be modified.

The use of nanostructured materials has been proposed to solve some of the problems currently associated with orthopedic implants [15]. In this connection, the nanostructured Ti, i.e., TiO_2 nanopore arrays (TNPA), has a great deal of interest [16–18]. In order to mimic the bioactive surface for dental and orthopedic implants, apatite (HAp) deposition is essential [19, 20]. It has been reported that alkaline pretreatment of anodized TiO_2 develops a secondary nanostructure on the material, thus, the sodium titanate layer was formed in the pretreated surface would accelerates and enhances the formation of the HAp and improves the bond strength of the coating with the substrate [21–23]. To the best of our knowledge, there are no such reports on the alkali treatment of TNPA.

Hence, the present work focuses on the modification of Ti surface into TNPA by anodization and the growth of HAp layer over its surface by in vitro immersion in Hank's solution. The influence of surface morphology, composition and crystallographic structure of the HAp on untreated Ti (UT) and TNPA were investigated using field emission

✉ N. Rajendran
nrajendran@annauniv.edu

1 Department of Chemistry, Anna University, Chennai 600 025, India

2 Present Address: Corrosion Science and Technology Division (CSTD), Indira Gandhi Center for Atomic Research, Kalpakkam 603 102, India

3 Materials Chemistry and Metal Fuel Cycle Group, Indira Gandhi Center for Atomic Research, Kalpakkam 603 102, India

scanning electron microscopic (FE-SEM) coupled with energy-dispersive X-ray spectroscopic (EDS), attenuated total reflectance Fourier transform infrared spectroscopic (ATR-FTIR), thin-film X-ray diffraction (TF-XRD) and X-ray photoelectron spectroscopic (XPS) techniques. In addition, in vitro biocompatibility and corrosion resistance of the specimens in Hank's solution were tested.

2 Materials and Methods

The Ti substrate (99.99%) used in this study was obtained from M/s Ti Anode Fabricators Pvt. Ltd, Chennai, India, in the form of sheet (0.11 cm^3). All chemicals used in the present experiments were of high-purity analytical reagent (AR) grade which include hydrofluoric acid (HF, 40%), glycerol, sodium hydroxide (NaOH, 97%), sodium chloride (NaCl, 99.9%), potassium chloride (KCl, 99.8%), calcium chloride (CaCl$_2$, 98%), sodium hydrogen carbonate (NaHCO$_3$, 99.8%), di-sodium hydrogen orthophosphate (Na$_2$HPO$_4$, 99%), magnesium chloride hexahydrate (MgCl$_2$·6H$_2$O, 99%), potassium dihydrogen orthophosphate (KH$_2$PO$_4$, 99%), magnesium sulfate heptahydrate (MgSO$_4$·7H$_2$O, 99.5%), and glucose. Double-distilled water was used for making electrolyte solutions.

2.1 Development of TNPA

The adapted anodization method in the present study was based on our earlier report [24]. Prior to anodization, the surface of Ti specimens was ground on both sides with SiC paper up to 1000 grit. Final polishing was done using alumina paste (1 μm size from M/s Chennai Metco Pvt. Ltd, Chennai, India) in order to produce a smooth surface. The polished specimen were washed, thoroughly rinsed with distilled water and were ultrasonically cleaned in a mixture of acetone, 2-propanol, and ethanol followed by pickling in a mixture of 0.9 M HF and 3.0 M HNO$_3$. Each specimen was rinsed with distilled water and dried in air at room temperature. All anodization experiments were carried out at room temperature using two-electrode electrochemical anodization cell consisting of Ti as anode and Pt (coupon, 1.08 cm^3) as cathode. Both the electrodes were connected to a direct current (DC) voltage source (Aplab, Model H0615) and anodization was carried out in a mixture of 0.15 M HF and 0.13 M glycerol at a constant voltage of 40 V for 1 h. After anodization, the specimens were rinsed in distilled water and dried.

2.2 Alkali and Heat Treatments and in vitro Biocompatibility Test

In order to shorten the time required for the formation of HAp and also to enhance the interfacial bonding strength

between TNPA and HAp layers, the TNPA specimen was treated with alkali (5 M NaOH) followed by heat treatment. The UT and TNPA specimens were immersed in 5 M NaOH solution at 50 °C for 30 min, then washed with distilled water, dried at room temperature in air, and annealed at 450 °C for 3 h.

The preparation procedure of Hank's solution is given elsewhere [25]. The UT and TNPA specimens were immersed in Hank's solution for different durations (3, 5 and 7 days) in a hanging configuration under static conditions. After exposure, the specimens were washed with doubled distilled water and dried in air and characterized.

2.3 Surface Characterization

The surface morphology and topography of the specimens were obtained using field emission scanning electron microscopic (FE-SEM, Supra 55-Carl-ZEISS, Germany) and atomic force microscopic (AFM, NT-MDT, Russia) techniques, respectively. All the topographical measurements were carried out in semi-contact mode. The pore dimensions (diameter and length of pore) were measured using AFM image analysis tools (NOVA Image Analysis software 1. 0. 26. 1443). Functional groups present on the surface of the specimens were identified using attenuated total reflectance–Fourier transform infrared spectroscopy (ATR-FTIR). The ATR-FTIR instrument used in the present study was Perkin Elmer spectrum Two, USA, and the spectra were obtained in the frequency range between 400 and 4000 cm^{-1}. The crystallinity of TNPA was found using thin-film X-ray diffraction (TF-XRD, BRUKER D8 Discover Optics, Germany) and laser Raman spectroscopic (LRS, Lab HR 800 spectrometer, HORIBA JOBIN–YVON make, Japan, Raman spectrometer equipped with 1800 grooves/mm holographic grating) techniques. In order to evaluate the HAp growth on TNPA, energy-dispersive X-ray spectroscopy with field emission scanning electron microscope (EDS) and X-ray photoelectron spectroscope (XPS, SPECS made XPS with Al K-α PSOI BOS-150, Germany) were used. The accuracy of the measured binding energy in the XPS analysis was ±0.3 eV.

2.4 Electrochemical Characterization

Electrochemical experiments were performed using a conventional three-electrode cell assembly maintained at 37 °C. Five neck ASTM standard electrochemical cell consisting of three-electrode system namely reference, counter and working electrodes used in the experiments were saturated Ag/AgCl, Pt sheet and test specimens, respectively.

Potentiodynamic polarization experiments were carried out for UT and TNPA specimens after immersion in

Hank's solution for different durations using Solartron 1287 Electrochemical Interface. The electrode potential was anodically scanned at a scan rate of 10 mV min^{-1}. In order to obtain reliable results, polarization experiments were triplicated in Hank's solution and all the measurements were almost reproducible. The polarization parameters such as corrosion current density (i_{corr}) and corrosion potential (E_{corr}) of each specimen were calculated from polarization curves with the aid of SAI Cview 2 software.

Electrochemical Impedance Spectroscopy (EIS) measurements were carried out using Solartron 1255 Frequency Response Analyzer (FRA) with Solartron 1287 electrochemical interface with the frequency ranging 10^4–10^{-2} Hz. The impedance response obtained over the applied frequency range was represented by Bode-impedance and Bode-phase angle plots. The EIS data was analyzed and fitted using an appropriate equivalent circuit by the SAI Zview 2 software.

3 Results and Discussion

3.1 Surface Characterization of TNPA

Figure 1a–f represents the 2D and 3D view of FE-SEM micrographs of UT and TNPA. From the morphological observation, it is obvious that the surface of UT showed only polishing grooves whereas, the TNPA exhibits self-assembled nanoporous structure. Almost the whole surface area of the TNPA surface attained similar morphology. Figure 2a, b shows the 2D line profile image (obtained for 3D FE-SEM image) and pore size distribution of TNPA. From the figure, it is apparent that the pore diameter and length of TNPA were in the range between 76–88 nm and 100–130 nm, respectively, and the average pore diameter and length were found to be 84 nm and 100 nm, respectively. The surface roughness of the specimens was measured from AFM topographs (Fig. 3a, b), which were found to be 155 nm and 250 nm for UT and TNPA, respectively. Higher surface roughness of TNPA was attributed to the formation of adherent nanoporous layer on Ti surface (evidenced from Figs. 1c–f, 2a, b). Several factors such as surface composition, roughness and wettability play an important role in implant–tissue interaction and osteo-integration [26]. The specimen with higher surface roughness results in early fixation and better mechanical stability for implants, which leads to good mechanical interlocking between the implant surface and bone in growth [27]. Deligianni et al. [28] reported that, the surface roughness influences the cellular response, which enhances the cells adhesion and proliferation. Lower surface roughness gives lesser bone contact [29]. Our earlier studies reported that, the surface roughness of 10 nm to 10 μm can influence the interface biology [10, 30].

Figure 4 shows the ATR-FTIR spectrum of TNPA. A weak band at 1630 cm^{-1} is ascribed to v_2 bending mode of O–H bond [31]. A strong broad band at 760 cm^{-1} is attributed to Ti–O stretching vibration in the TiO$_2$ film [32]. The presence of O–H bond on the TiO$_2$ layer is due to the presence of Ti–OH at the solid–liquid interface. The negatively charged sites present on TiO$_2$ surface attracts positively charged Ca^{2+} ions, followed by the arrival of phosphate ions and forms HAp [33]. The surface morphology change is very much related to the crystal growth and phase transition. Hence, TF-XRD was used to investigate the effect of crystal growth and phase transition on the morphology of TNPA. The TF-XRD pattern of the TNPA is represented in Fig. 5. It was observed that the TNPA annealed at 450 °C for 3 h exhibited anatase crystal phase with characteristic anatase peaks at 2θ values of 25.4° and 48.2° (JCPDS No: 21-1272), which correspond to the plane of (101) and (200), respectively. The TF-XRD results are in accordance with the previous report [34].

The crystallite size of the anatase TiO$_2$ was ∼29 nm which was calculated using Scherrer formula (Eq. 1):

$$L = K\lambda/\beta \cos\theta \qquad (1)$$

where L, K, λ, θ and β are crystallite size, Scherrer constant (0.89), wave length (1.54 Å), diffraction angle and full width at half maximum of the diffraction peak, respectively.

In order to further confirm the crystalline nature of TNPA beyond doubt, LRS was taken after the heat treatment of TNPA which is given in Fig. 6. The spectrum showed four well resolved peaks at 147.5 cm^{-1} (E_g), 405.5 cm^{-1} (B_{1g}), 518.7 cm^{-1} (A_{1g}) and 642.7 cm^{-1} (E_g) which are due to the anatase nature of the surface. It has been reported that the characteristic vibrations of anatase phase were at 147.5 cm^{-1} (E_g), 200 cm^{-1} (E_g), 397.5 cm^{-1} (B_{1g}), 520 cm^{-1} (A_{1g}) and 641 cm^{-1} (E_g) [35]. The Raman result supported well with TF-XRD result. Electrochemically grown and heat-treated TNPA having anatase structure are expected to be a good precursor system for the formation of HAp [36].

3.2 In Vitro Characterization of TNPA

The biocompatibility of the specimen is determined by its HAp forming ability when immersed in body fluids. In order to assess the biocompatibility of UT and alkali heat-treated TNPA specimens, they were immersed in Hank's solution for different durations such as 3, 5, and 7 days. The FE-SEM and EDS studies were employed to investigate the morphology and elements present on the surface of the specimens, respectively. Figure 7a–f displays the FE-SEM images and EDS spectra of UT after immersion in Hank's solution for 3, 5, and 7 days. It could be observed
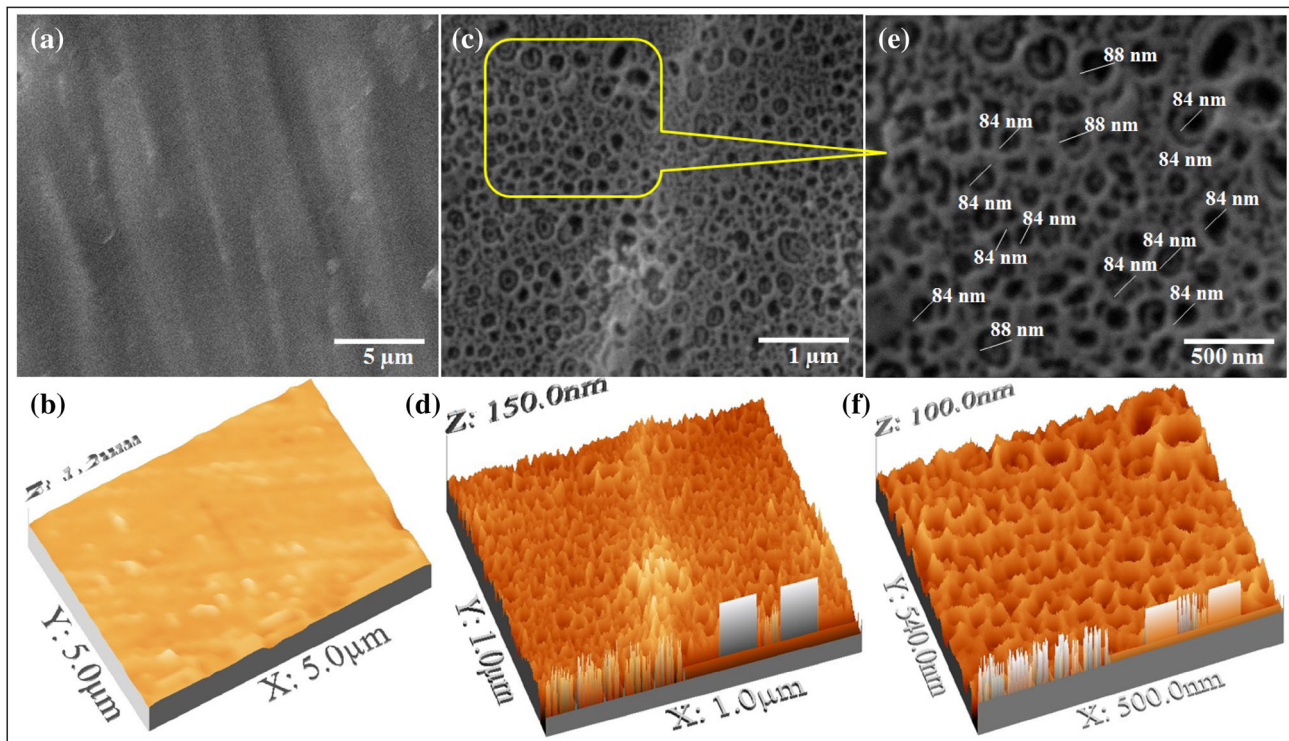
Fig. 1 FE-SEM micrographs and the 3D images obtained from FE-SEM micrographs of **a**, **b** UT, **c**, **d** TNPA and **e**, **f** at higher magnification images of TNPA
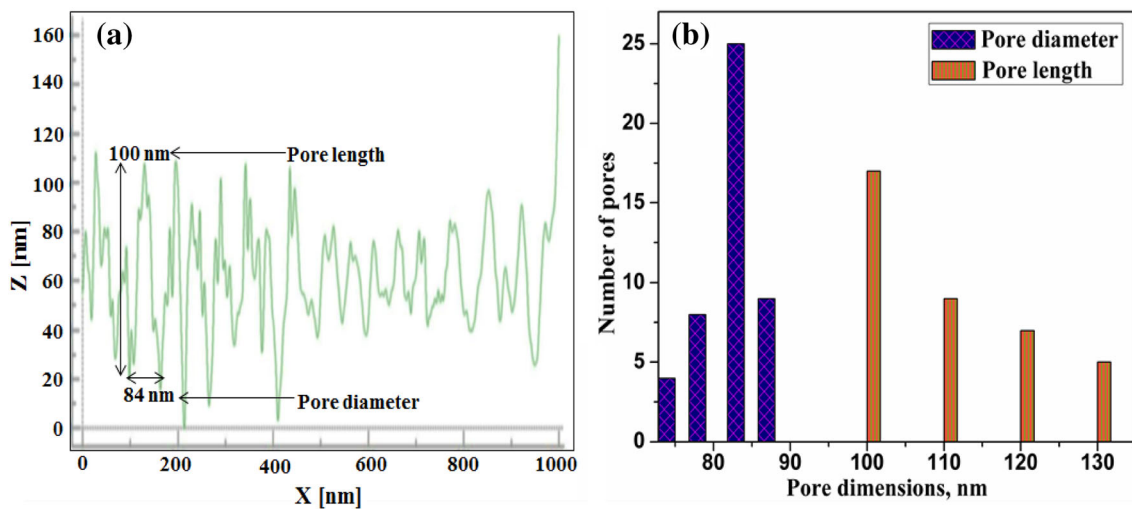
Fig. 2 **a** 2D line profile of the TNPA (obtained for 3D FE-SEM image) and **b** Pore size distribution (obtained from 2D line profile analysis) of TNPA

that the surface of UT shows only polishing grooves with very little white particles scattered on the surface after 3 and 5 days of immersion in Hank's solution whereas, after 7 days of immersion few HAp like new particles formed randomly over the surface. EDS spectra showed only the presence of Ti and O for 3 and 5 days of immersion, whereas, after 7 days of immersion, Ca and P was also present along with Ti and O. From the EDS spectrum, it

could be confirmed that Ca and P was present over the surface, indicating HAp formation on the Ti surface on prolonged immersion in Hank's solution.
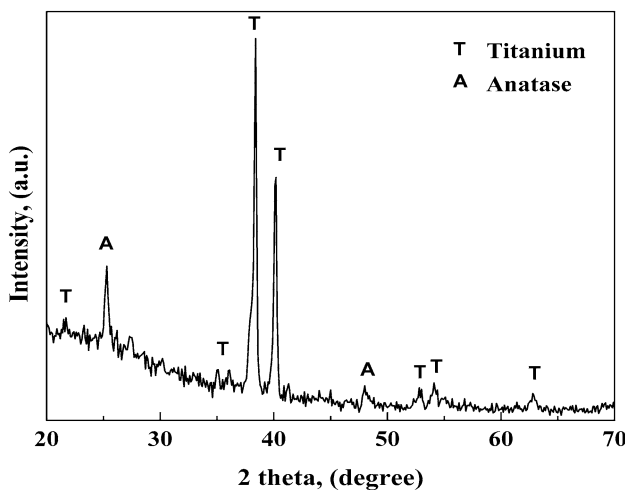
Figure 8a–f shows the FE-SEM micrographs and EDS spectra of alkali heat-treated TNPA after immersion in Hank's solution for different durations (3, 5 and 7 days). The TNPA specimens after immersion for 3 and 5 days of immersion showed white particles which do not fully cover

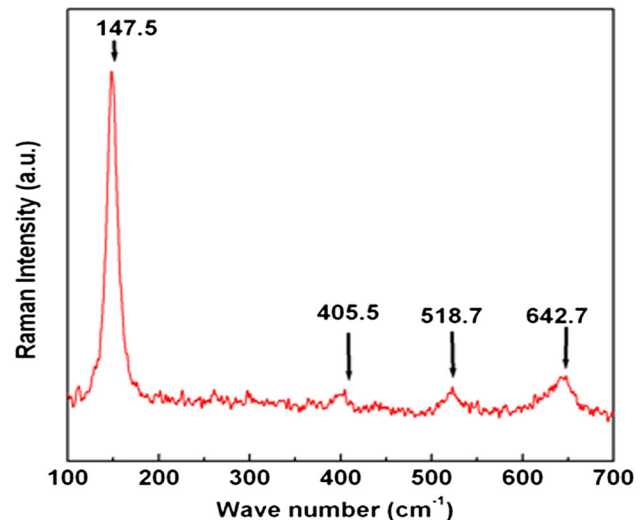**Fig. 3** AFM topographs of **a** UT and **b** TNPA
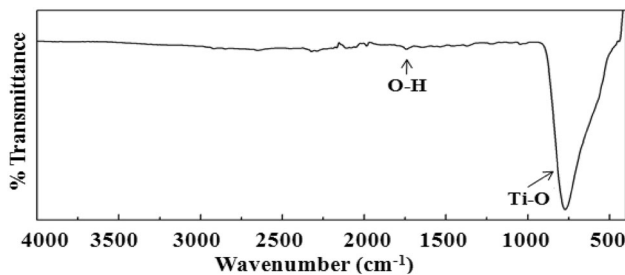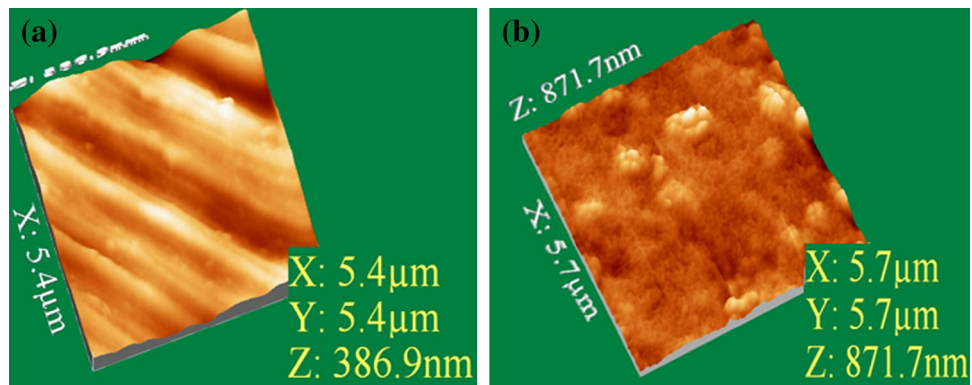
Fig. 4 ATR-FTIR spectra of anodized annealed TNPA

Fig. 5 TF-XRD pattern anodized annealed TNPA

Fig. 6 Raman spectrum of anodized annealed TNPA

the surface. Further increase in the immersion time to 7 days showed the complete coverage of fiber web-like morphology. This new layer contains Ca and P as shown by the EDS. In addition to these elements, a trace of Mg is also present on the surface of the specimen. It has been reported that, Mg^{2+} and Na^+ ions might substitute Ca^{2+} ions in HAp, which is in line with the composition of biological HAp from human bones. The natural bone contains traces of ions such as Mg^{2+} and Na^+, as well as CO_3^{2-}, HPO_4^{2-}, F^- and Cl^- [34]. From the above results, it is confirmed that the UT showed only partial coverage of

HAp even after 7 days of immersion, whereas, in the case of TNPA, the entire surface was covered with HAp. The formation of HAp is further confirmed by ATR-FTIR, TF-XRD, and XPS studies.

The ATR-FTIR was used to find out the functional groups such as phosphate, carbonate, and other functional groups related to HAp present on the surface of the specimens. Figure 9a–c shows ATR-FTIR spectra of alkali heat-treated TNPA after immersion in Hank's solution for different durations. Small vibrational bands at 1639 and 1032 cm^{-1} were observed after 3 days of immersion, which were recognized as adsorbed water and phosphate group, respectively. A strong band at 759 cm^{-1} is attributed to Ti–O stretching. Broad absorption bands at 3663–3048 and 1639 cm^{-1} obtained after 5 days of immersion in Hank's solution are due to the stretching and bending mode of adsorbed H_2O, respectively, in crystalline HAp [37]. After 7 days of immersion in Hank's solution, a sharp band due to the P–O and v_3 asymmetric stretching mode of the PO_4^{3-} group was found in the region of

Fig. 7 FE-SEM morphology and EDS spectra of UT after immersion in Hank's solution: **a**, **b** 3 days, **c**, **d** 5 days and **e**, **f** 7 days
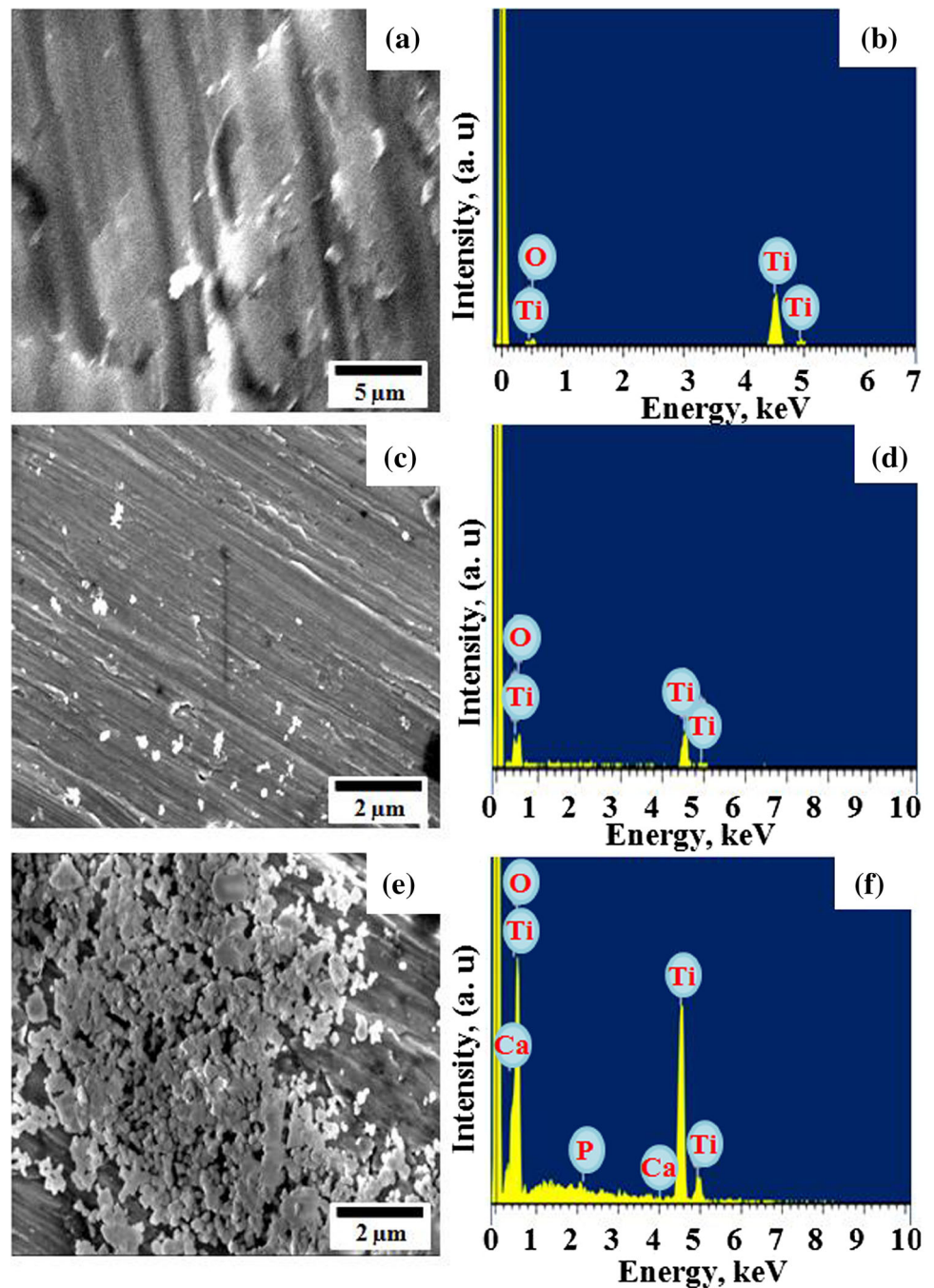
1026 cm^{-1}. The v_4 and v_2 degenerated bending modes of phosphates (O–P–O bonds) were found at 602 and 559 cm^{-1}, respectively [38]. The bands detected at 1425 and 875 cm^{-1} were assigned to the CO_3^{2-} group of B-type carbonated HAp, where PO_4^{3-} groups are substituted by CO_3^{2} groups [39]. The band due to Ti–O stretching was not observed after 7 days of immersion which suggests that the TNPA surface was densely packed with HAp layer which has already been confirmed by FE-SEM images and EDS spectra.

The characteristic vibrations of phosphate and carbonate were observed for all the specimens; however, the intensity of bands were very less after 3 and 5 days of immersion, whereas, after 7 days of immersion, very strong characteristic vibrational bands of phosphate and carbonates were observed. Hence, the appearance of the phosphate and carbonate absorption bands in the spectra of TNPA after immersion in Hank's solution confirmed the formation of carbonated HAp layer over TNPA. The formation of HAp is described in Eq. (2).

Fig. 8 FE-SEM morphology and EDS spectra of alkali heat-treated TNPA after immersion in Hank's solution: **a, b** 3 days, **c, d** 5 days and **e, f** 7 days

$$10Ca^{2+} + 6PO_4^{3-} + 2OH^- \rightarrow Ca_{10}(PO_4)_6(OH)_2 \qquad (2)$$
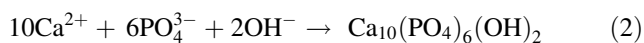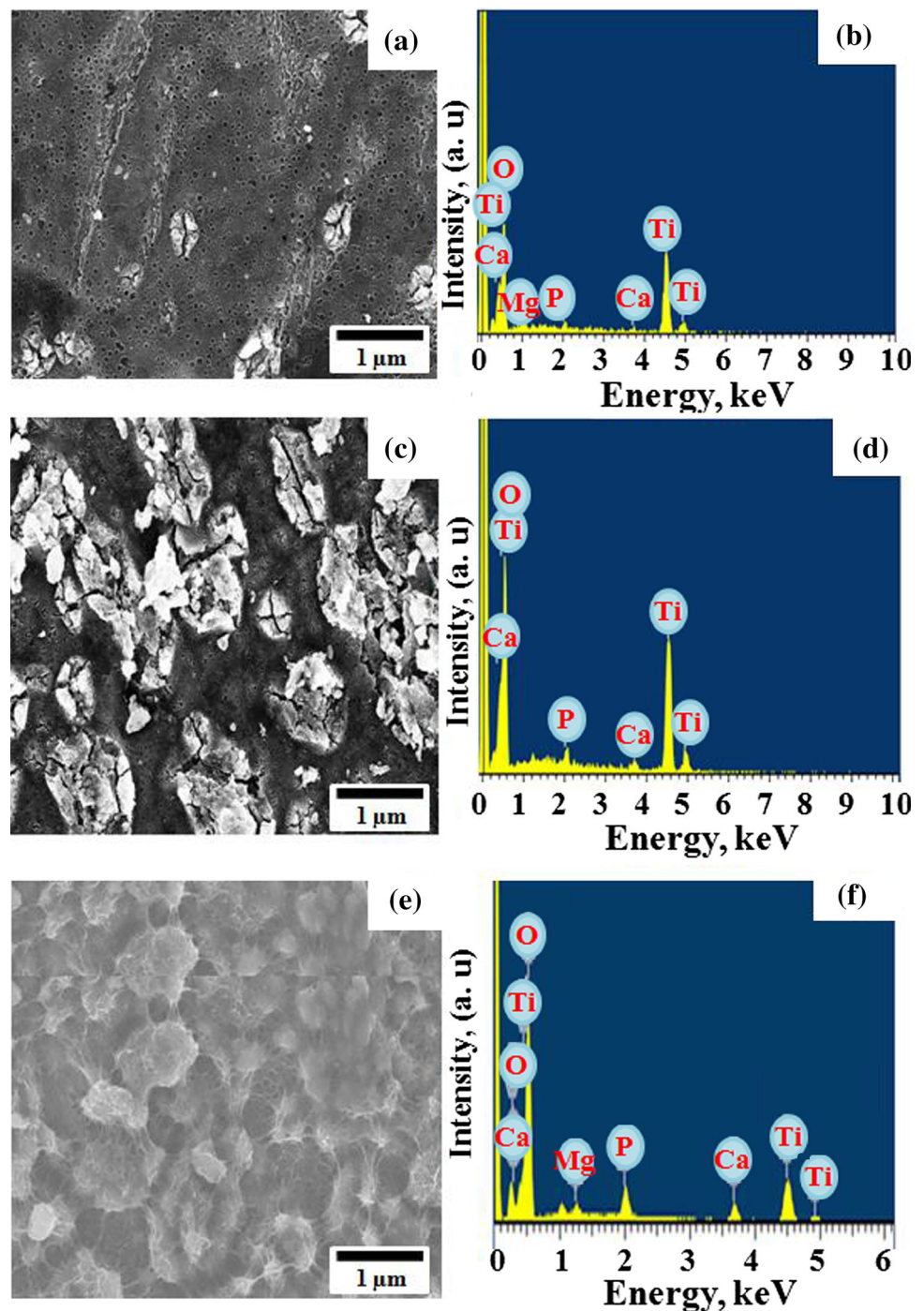
The above observation clearly reveals the growth of HAp layer, which is essentially the carbonated HAp, resembling that of human tissues.

From the FE-SEM, EDS, and ATR-FTIR studies, it is obvious that 3 and 5 days' time is very short to grow the HAp on the entire surface of TNPA, and 7 days' time is enough for the growth of HAp on the entire surface. Hence,

the TF-XRD and XPS studies were taken only for TNPA after 7 days of immersion in Hank's solution, i.e., after the growth of HAp on the entire TNPA surface. Figure 10 shows the TF-XRD pattern of TNPA after 7 days of immersion in Hank's solution. The characteristic peaks of HAp were seen to occur at 2θ values of 25.9°, 29.3°, 31.5°, 32.1°, 33.1°, 34.1°, 42.1°, 46.8° and 49.1° corresponding to the planes (002), (210), (211), (112), (300), (202), (311), (222), and (213) which are consistent with the standard
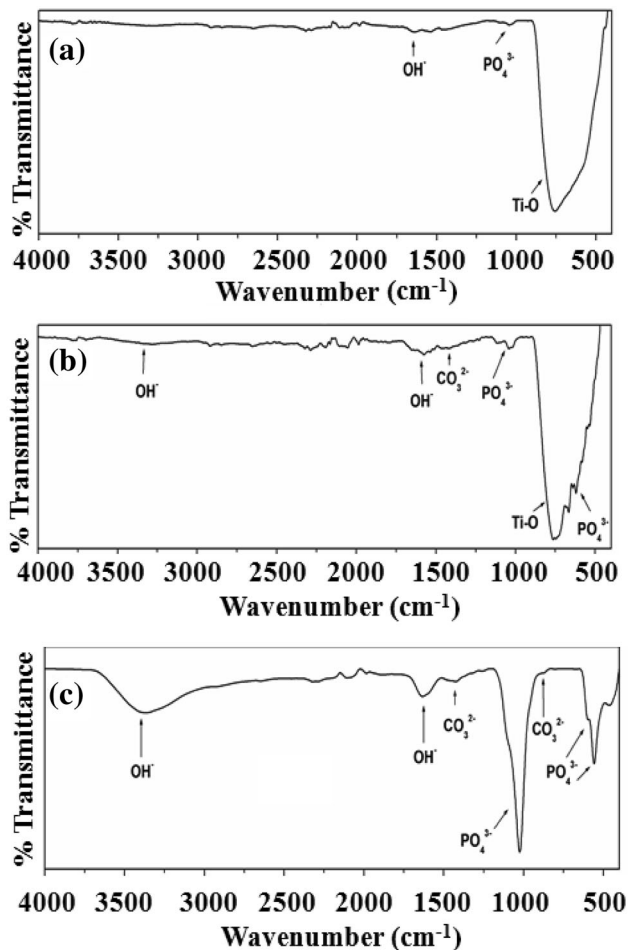
Fig. 9 ATR-FTIR spectra of TNPA after immersion in Hank's solution: **a** 3 days, **b** 5 days and **c** 7 days

XRD peaks for HAp (JCPDS-09-0432) [40]. It has been reported that, the amorphous calcium phosphate is metastable which is ultimately transformed into crystalline
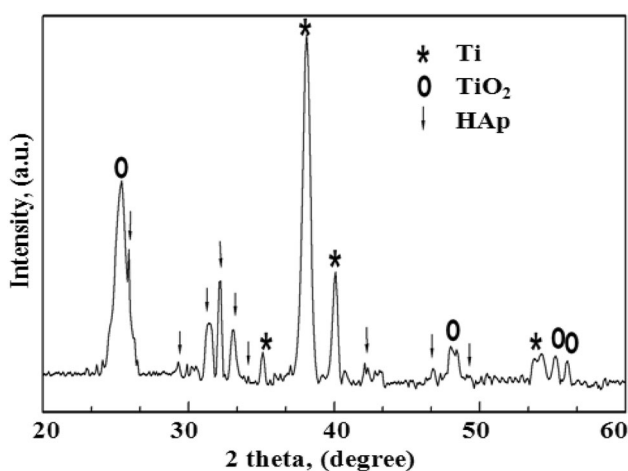
Fig. 10 TF-XRD pattern of alkali heat-treated TNPA after 7 days immersion in Hank's solution

bone-like HAp [41]. Longer period of immersion in body fluid leads to the formation of an amorphous phosphate [42]. Hence, the new phase formed on TNPA surface after the immersion in Hank's solution was considered to be bone-like HAp [43, 44].

The XPS spectra for O, C, Ca and P of TNPA after 7 days of immersion in Hank's solution are shown in Fig. 11a–d. By curve fitting analysis, the O 1 s spectrum was deconvoluted into two Gaussian component peaks at the binding energy values of 530.8 and 533.5 eV, which correspond to oxygen in phosphate group (PO_4^{3-}) and adsorbed water, respectively [45]. The C 1 s spectrum was also deconvoluted into two peaks at 285.4 and 287.5 eV, which are attributed to COO^- bond. The Ca 2p peaks at 347.9 and 351.3 eV correspond to a divalent oxidation state (Ca^{2+} as Ca $2p_{3/2}$ and the Ca $2p_{1/2}$) in calcium oxygen compounds. This confirmed that the Ca is present as calcium phosphate [46, 47]. The P 2p peak at 134.3 eV is attributed to the presence of phosphates ($H_2PO_4^-$) and the higher binding energy of P 2p at 137.1 eV is due to the Ca and P compounds [48]. The Ti has a greater tendency to bind with oxygen of the phosphate, and thus, interaction between the Ti^{4+} and mineral phase takes place, which leads to the formation of calcium titanium mixed oxide phase. These results clearly confirmed the formation of carbonated HAp layer over TNPA surface.

3.2.1 Electrochemical Characterization of TNPA

Besides the biocompatibility, corrosion resistance is also an important requirement for any implant material. If a material possess good biocompatibility but not having required resistance toward corrosion will spontaneously fail in long run. In order to evaluate the corrosion resistance of the TNPA specimens after immersion in Hank's solution for different durations (immediate, 3, 5 and 7 days), they were subjected to potentiodynamic polarization and EIS studies. The potentiodynamic polarization curves of UT and alkali heat-treated TNPA after immediate, 3, 5 and 7 days of immersion in Hank's solution is given in Fig. 12a–d. Polarization parameters such as corrosion potential (E_{corr}) and corrosion current density (i_{corr}) values of UT and alkali heat-treated TNPA specimens after immediate, 3, 5 and 7 days of immersion in Hank's solution are shown in Table 1, which were calculated using the SAI Cview software. Since the potential range is more, the Tafel domain is not visible in the polarization curves. The inset in Fig. 12a shows the enlarged polarization curve of TNPA. When compare to third day of immersion, the E_{corr} value was decreased for 5th day of immersion in TNPA samples, this is because on the third day, the HAp growth was very less on the TNPA surface, whereas, on the fifth day, rapid nucleation and growth of HAp was observed (as

Fig. 11 XPS spectra of alkali heat-treated TNPA after 7 days of immersion in Hank's solution: **a** O 1 s, **b** C 1 s, **c** Ca 2p and **d** P 2p
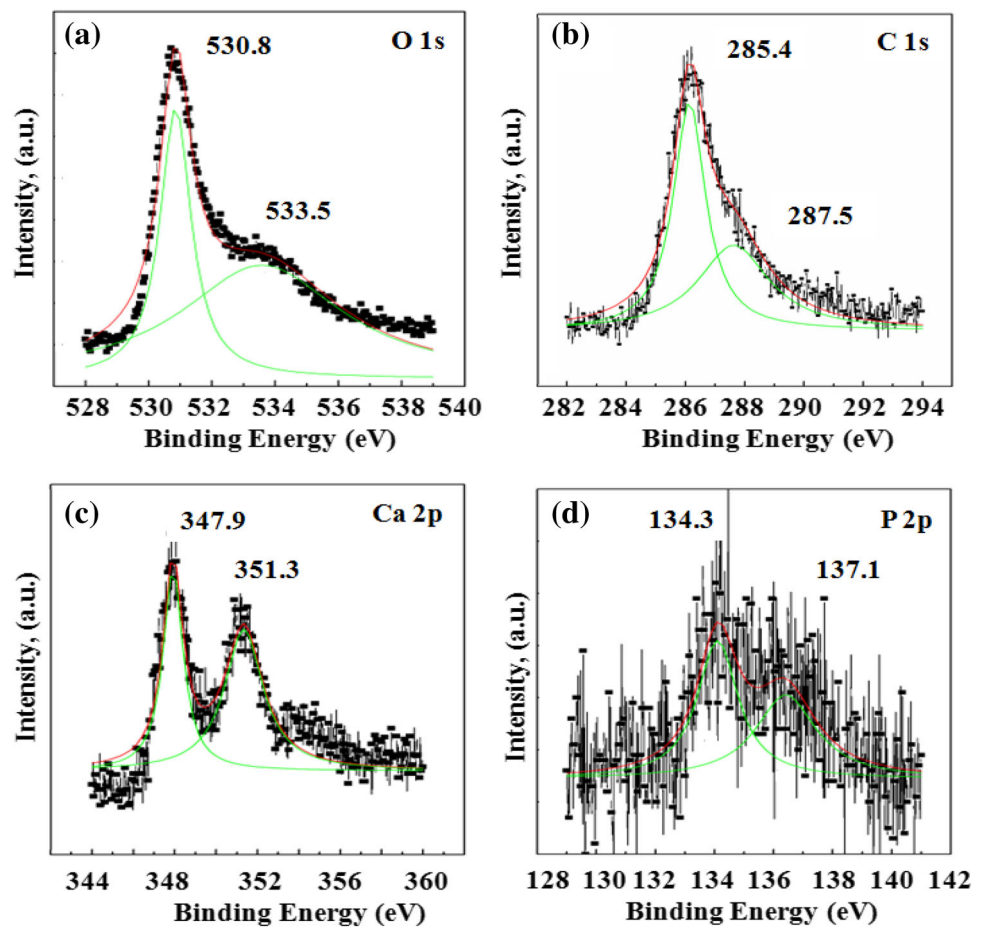

evidenced from FE-SEM images), which means that there has been increased movement of Ca and P ions on the surface. However, on the seventh day the surface was entirely covered by newly formed HAp layer, which prevents the corrosive ions in Hank's solution from reaching the TNPA surface and hence, the E_{corr} was shifted to the nobler direction. Fluctuation in the current density in the potential range between 0.6 and 1.1 V was observed for TNPA specimens after 3 and 5 days of immersion, which may be due to the presence of unstable dissolution and re-filming of the new surface layer [43]. The increase in current density of TNPA may be associated with the oxygen evolution reaction [49].

In comparison with UT, alkali heat-treated TNPA specimens showed an increase in corrosion resistance of one order of magnitude. It could be observed that, the alkali heat-treated TNPA after 7 days of immersion in Hank's solution exhibited higher E_{corr} and lower i_{corr} values when compared to other specimens. Such an increase in potential is attributed to the presence of densely packed HAp on the surface which is in accordance with the ATR-FTIR results. These results revealed that the TNPA after immersion in Hank's solution for 3, 5 and 7 days possessed excellent

corrosion resistance with very low i_{corr} compared to UT. Anodization provides a porous passive film which restricts the movement of metal ions from metal surface to the solution [50]. The pores act perfectly as passive pits due to the higher barrier oxide thickness and compact pore walls. Therefore, the effective surface area was increased for the nanopatterned surface, and it provides the environment for the possible surface reaction of HAp nucleation [51]. Overall, the alkali heat-treated TNPA specimen after 7 days immersion in Hank's solution showed better corrosion resistance compared to 3 and 5 days of immersion.

Electrochemical impedance spectroscopy was used to characterize the oxide films on the surface and to study the resistance of passive surface films [52]. The EIS spectra of UT and alkali heat-treated TNPA after immediate, 3, 5, and 7 days of immersion in Hank's solution are shown in Fig. 13a–h. The Bode plots for UT and alkali heat-treated TNPA showed phase angle values around −81° and −79°, respectively, and remained constant over a wide range of frequency after immediate immersion in Hank's solution, indicating highly capacitive behavior of the passive oxide film formed on their surfaces [53]. The UT surface is very smooth and even, whereas the TNPA surface is rough and
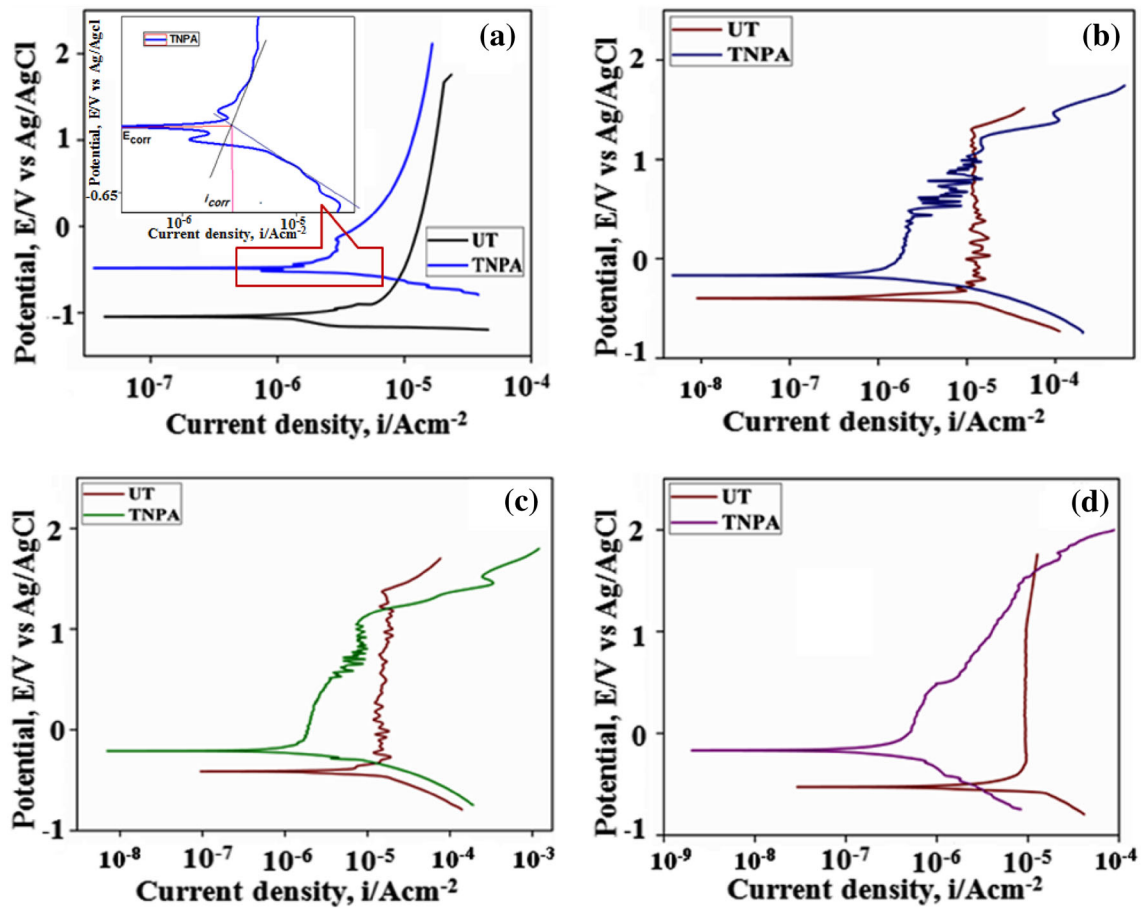
Fig. 12 Potentiodynamic polarization curves of UT and alkali heat-treated TNPA after immersion in Hank's solution: **a** immediate, (*inset enlarged curve of TNPA*) **b** 3 days, **c** 5 days and **d** 7 days

Table 1 Polarization parameters of UT and alkali heat-treated TNPA after immediate, 3, 5 and 7 days of immersion in Hank's solution

Specimen	Duration (days)	I_{corr} (Acm^{-2})	$-E_{corr}$ (V)
UT	Immediate	$1.41 \pm 0.25 \times 10^{-5}$	1.04 ± 0.50
	3	$1.35 \pm 0.14 \times 10^{-5}$	0.49 ± 0.12
	5	$1.21 \pm \times 10^{-5}$	0.40 ± 0.09
	7	9.02×10^{-6}	0.21 ± 0.10
TNPA	Immediate	5.6×10^{-6}	0.41 ± 0.15
	3	4.19×10^{-6}	0.16 ± 0.10
	5	3.75×10^{-6}	0.53 ± 0.08
	7	1.93×10^{-6}	0.13 ± 0.11

porous which allows the solution to reach the Ti surface via pores. This may be the reason for marginally lower phase angle value of TNPA surface. After 7 days of immersion, the phase angle plot of UT exhibited two distinct behaviors and attained a maximum value of $-77°$ at the intermediate frequency region, whereas, for the alkali heat-treated TNPA specimen, the phase angle plot showed three distinct

behaviors, which indicates that a new layer is formed after immersion. The formed new layer is attributed to the HAp layer as evidenced from EDS, ATR-FTIR, TF-XRD, and XPS results.

In order to theoretically evaluate the passive oxide film on the surface of the specimens after immersion in Hank's solution for immediate, 3, 5, and 7 days, EIS spectra was fitted with the equivalent circuit models which are shown in Fig. 14a–d. Some previous papers reported this specific equivalent circuit model for fitting the EIS spectra obtained for porous titania samples [54, 55], and the same model was followed in the present study to fit the EIS spectra. Although the material is porous, if the characteristics of layers present on the substrate surface are different, then the series RC circuits were used to fit the data. Hence, the equivalent circuit model used in the present study to fit for UT after immediate, 3 and 5 days of immersion is composed with series combination of $R_sR_bQ_b$ (Fig. 14a) and 7 days of immersion is composed with $R_sR_bQ_bR_aQ_a$ (Fig. 14b), where, R_s denotes solution resistance, R_b and Q_b are the polarization resistance and double layer capacitance of the barrier layer, respectively, and R_a and Q_a are the
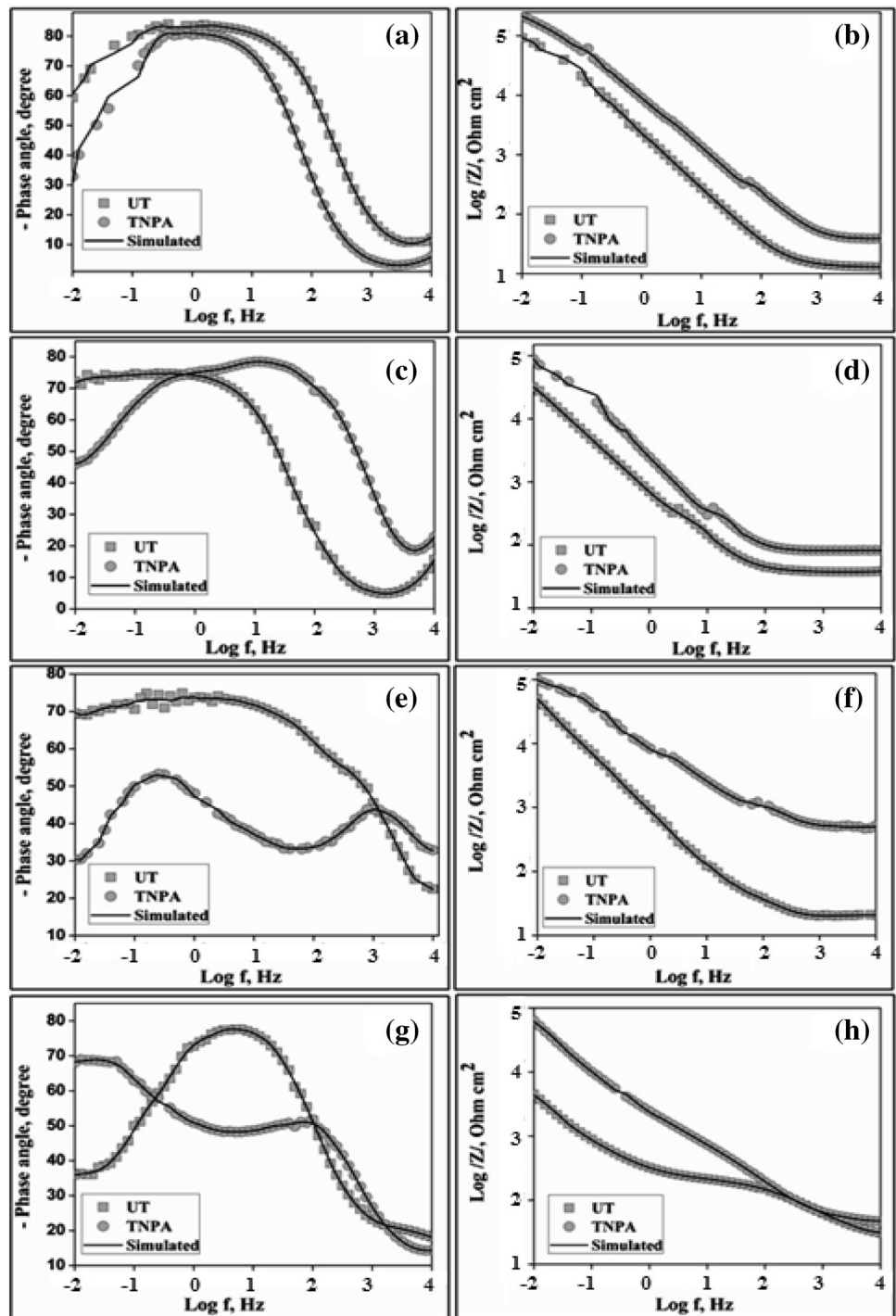
polarization resistance and the double layer capacitance of HAp layer, respectively.

The impedance plot of UT after immersion in Hank's solution for 3 and 5 days showed single time constant, whereas 7 days of immersion showed two time constants, which was attributed to the inner barrier layer and outer HAp layer. The impedance parameters are tabulated in Table 2. From the table, the frequency independent parameter n_b is 0.92 indicating a near capacitive behavior of the passive oxide film formed on UT surface. This suggested that the behavior of surface layer approached that of an ideal capacitor [56]. It has been reported that nucleation and growth of bone-like HAp formed on UT surface on long period of immersion in body fluid solution [49].

Figure 14c gives the equivalent circuit after immediate and 3 days of immersion of alkali heat-treated TNPA,

Fig. 14 Equivalent circuits of **a** UT after immediate, 3, 5 days, **b** UT after 7 days, **c** alkali heat-treated TNPA after immediate, 3 days and **d** alkali heat-treated TNPA after 5, 7 days immersion in Hank's solution
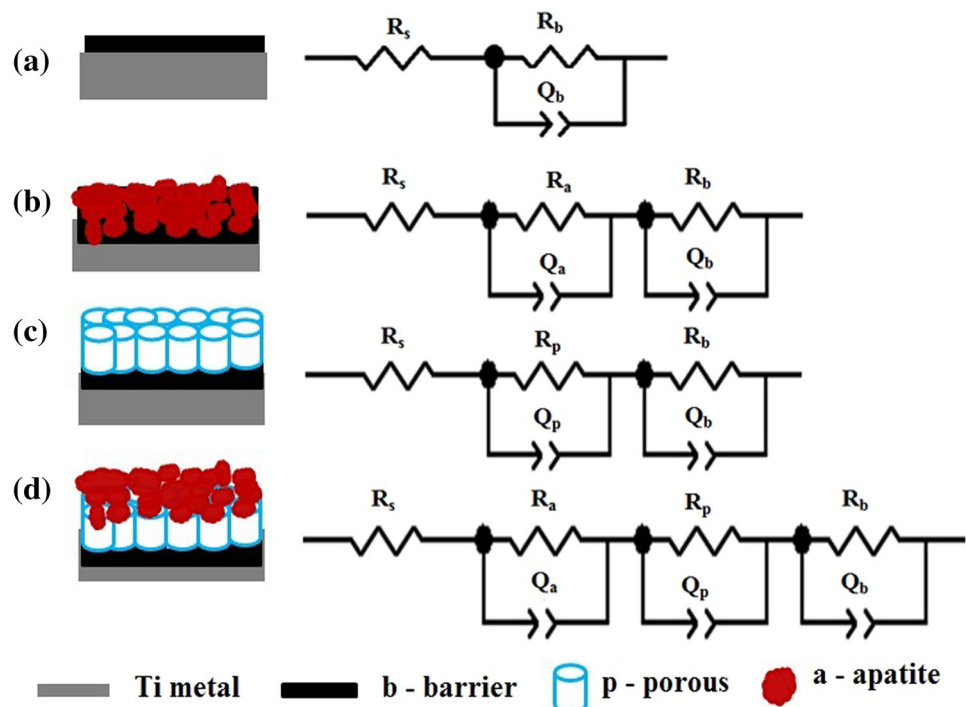
Table 2 EIS parameters of UT after immediate, 3, 5 and 7 days of immersion in Hank's solution

Duration (days)	R_s	R_a	Q_a	n_a	R_b	Q_b	n_b
Immediate	0.01 (0.002)	–	–	–	232 (9)	4.2 (0.16)	0.92 (0.025)
3	0.01 (0.001)	–	–	–	250 (3)	5.1 (0.24)	0.92 (0.001)
5	0.03 (0.015)	–	–	–	256 (8)	4.5 (0.09)	0.90 (0.004)
7	0.02 (0.001)	0.90 (0.11)	4.5 (0.30)	0.65 (0.006)	245 (5)	1.1 (0.12)	0.86 (0.006)

Values mean (standard deviation), R_s, R_a and R_b (k Ω cm^2), Q_a and Q_b ($Fcm^{-2}S^n$) $\times 10^{-5}$

where, R_b, R_p, Q_b, and Q_p represent the polarization resistance and double layer capacitance of the barrier and porous layers, respectively. The formation of nanoporous outer layer is expected to promote ion incorporation and molecular absorption which can result in strong adhesion between the implant and the adjacent tissue [57]. It has been reported elsewhere that the corrosion resistance of Ti alloy is ascribed to the inner barrier layer and the ability to osteo-integrate is attributed to the outer porous layer [58]. The porous oxide can become hydrated and ions from body fluid can easily incorporate into the pores and further precipitation leads to self-healing.

Based on the EIS spectra, three layer model (Fig. 14d) was used to interpret the obtained spectra for alkali heat-treated TNPA after 5 and 7 days of immersion. In this model, R_b, R_p, and R_a represent the polarization resistance of the barrier, porous, and HAp, layers, respectively. Q_b, Q_p and Q_a are the double layer capacitance of barrier, porous and HAp layers, respectively. The obtained impedance parameters are tabulated in Table 3. The n_p values of the specimen were close to 1, which meant that the porous layer behaved as ideal capacitor. The R_b was found to be 1300 kΩ cm^2 after 3 days of immersion, and it decreased with increase in immersion time. The R_a and Q_a values gradually increased with increase in the immersion time which is due to the increased coverage of HAp layer [59].

From the equivalent circuit parameters, it is obvious that the polarization resistance of the TNPA greatly improved after 7 days of immersion compared to 3 and 5 days of immersion, which has not been observed for UT. Apart from this, the capacitive value of the porous film was very low after 7 days of immersion compared to that obtained after 3 and 5 days of immersion which indicates the insulating property of the porous film. The high polarization resistance and low capacitance values confirmed the existence of superior protective layer, i.e., the formation HAp layer on the surface. The presence of third time constant after 7 days of immersion in Hank's solution is an

Table 3 EIS parameters of alkali heat-treated TNPA after immediate, 3, 5, and 7 days of immersion in Hank's solution

Duration (days)	R_s	R_a	Q_a	n_a	R_p	Q_p	n_p	R_b	Q_b	n_b
Immediate	0.01 (0.003)	–	–	–	0.05 (0.01)	1.0 (0.02)	0.99 (0.001)	396.09 (72)	2.9 (0.14)	0.84 (0.002)
3	0.21 (0.015)	–	–	–	6.16 (0.15)	1.8 (0.04)	0.96 (0.015)	1300 (220)	3.9 (0.23)	0.80 (0.001)
5	0.04 (0.001)	1.10 (1.0)	1.6 (0.5)	0.72 (0.01)	8.72 (0.02)	2.7 (0.01)	0.97 (0.005)	1296 (245)	3.4 (0.05)	0.62 (0.011)
7	0.03 (0.001)	7.25 (1.5)	3.6 (0.3)	0.75 (0.03)	9.70 (0.23)	4.4 (0.08)	0.99 (0.002)	1068 (150)	2.2 (0.20)	0.85 (0.010)

Values mean (standard deviation), R_s, R_a and R_b (k Ω cm^2), Q_a and $Q_p (Fcm^{-2}S^n) \times 10^{-7}$, Q_b (Fcm$^{-2}S^n$) $\times 10^{-6}$

indication that Ca and P ions present in the Hank's solution interact and deposit on alkali heat-treated TNPA surface. Wang and Wang reported that the nucleation and growth of bone-like HAp takes place on chemically treated Ti surface on prolonged immersion in simulated body fluid solution [60].

From the above results, it is confirmed that, after 7 days of immersion in Hank's solution, the alkali heat-treated TNPA surface is covered with HAp layer and showed an excellent biocompatibility and corrosion resistance. The obtained results were also evidenced from EDS, ATR-FTIR, TF-XRD, and XPS analysis, which are schematically represented in Fig. 15. There are three major steps involved in this process, which include anodization, in vitro biocompatibility test, and electrochemical corrosion studies. Hence, Ti with nanopore arrays could be used as a viable implant material with enhanced biocompatibility and corrosion resistance in vitro.
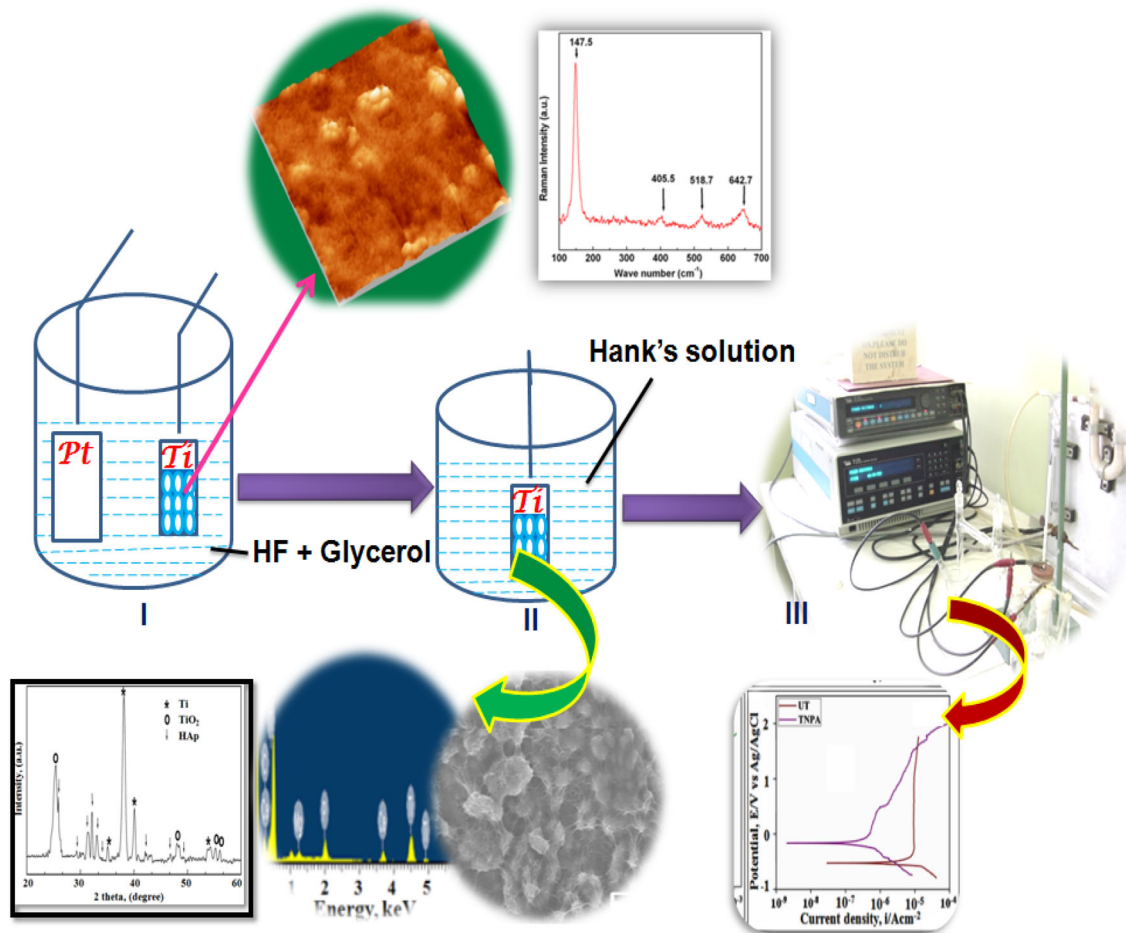
Fig. 15 Schematic representation of the summary of the present investigation

4 Conclusions

The TNPA with the pore diameter of approximately 85 nm was developed on Ti via simple electrochemical anodization method using fluoride containing viscous organic electrolyte. The surface morphological and elemental composition studies showed that, the HAp layer was grown on both UT and TNPA surfaces by in vitro immersion in Hank's solution. When compare to the UT surface, all the TNPA specimens after immersion in Hank's solution showed enhanced biocompatibility and high corrosion resistance. In conclusion, our results showed that the TNPA is an interesting material, which offers the required biocompatibility in the body fluids, thus making it applicable for orthopedic implants.

Compliance with Ethical Standards

Conflict of interest There is no conflict of interest in this paper.

References

1. Eliaz N, Sridhar TM, Mudali UK et al (2005) Electrochemical and electrophoretic deposition of hydroxyapatite for orthopaedic applications. Surf Eng 21:1–5
2. Amin MS, Randeniya LK, Bendavid A et al (2010) Apatite formation from simulated body fluid on various phases of TiO_2 thin films prepared by filtered cathodic vacuum arc deposition. Thin Solid Films 519:1300–1306
3. Dey T, Roy P, Fabry B et al (2011) Anodic mesoporous TiO_2 layer on Ti for enhanced formation of biomimetic hydroxyapatite. Acta Biomater 7:1873–1879
4. Mudali UK, Sridhar TM, Raj Baldev (2003) Corrosion of bio implants. Sadhana 28:601–637
5. Geetha M, Mudali UK, Gogia AK et al (2004) Influence of microstructure and alloying elements on corrosion behavior of Ti–13Nd–13Zr alloys. Corros Sci 46:877–892
6. Hamlekhan A, Sinha-Ray S, Takoudis C et al (2015) Fabrication of drug eluting implants: study of drug release mechanism from titanium dioxide nanotubes. J Phys D Appl Phys 48:275401
7. Hamlekhan A, Butt A, Patel S et al (2014) Fabrication of anti-aging TiO_2 nanotubes on biomedical Ti alloys. PLoS ONE 9(5):e96213
8. Faverani LP, Fogac JF, Machado T et al (2015) Does surface topography improve electrochemical behavior of Ti–6Al–4 V alloy in different saliva pH levels? J Bio Tribo Corros 1:20. doi:10.1007/s40735-015-0020-1
9. Huang W, Wang Z, Liu C et al ((2015) Wear and Electrochemical Corrosion Behavior of Biomedical Ti–25Nb–3Mo–3Zr–2Sn Alloy in Simulated Physiological Solutions. J Bio Tribo Corros 1:1, doi:10.1007/s40735-014-0001-9
10. Indira K, Mudali UK, Rajendran N (2013) Corrosion behavior of electrochemically assembled nanoporous titania for biomedical applications. Ceram Int 39:959–967
11. Souza JCM, Tajiri HA, Morsch CS et al (2015) Tribocorrosion behavior of Ti_6Al_4V coated with a bio-absorbable polymer for biomedical applications. J Bio Tribo Corros 1:27. doi:10.1007/s40735-015-0029-5
12. Cruz HV, Henriques M, Teughels W et al (2015) Combined Influence of fluoride and biofilms on the biotribocorrosion behavior of titanium used for dental applications. J Bio Tribo Corros 1:1–12. doi:10.1007/s40735-015-0021-0
13. Kunze J, Muller L, Macak JM et al (2008) Time—dependent growth of biomimetic apatite on anodic TiO_2 nanotubes. Electrochim Acta 53:6995–7003
14. Souza JCM, Henriques M, Teughels W et al (2015) Wear and corrosion interactions on titanium in oral environment: literature review. J Bio Tribo Corros 1:13. doi:10.1007/s40735-015-0013-0
15. Kim D, Fujimoto S, Schmuki P et al (2008) Nitrogen doped anodic TiO_2 nanotubes grown from nitrogen containing Ti alloys. Electrochem Commun 10:910–913
16. Huang L, Peng F, Yu H et al (2010) The influence of ultrasound on the formation of TiO_2 nantube arrays. Mater Res Bull 45:200–204
17. Indira K (2015) Development of titanium nanotube arrays for orthopaedic applications. Dissertation, Anna University, http://shodhganga.inflibnet.ac.in/handle/10603/37614
18. Indira K, Ningshen S, Mudali UK et al (2013) Effect of anodization temperature on the surface morphology of anodized titanium. In: Jayakumar S, Kannan MD, Balasundaraprabhu R, Prassana S (eds) Thin film and nanomaterials. Macmillan publishers India Limited, Mumbai, pp 63–66
19. Sridhar TM, Mudali UK, Subbaiyan M (2003) Preparation and characterization of electrophoretically deposited hydroxyapatite coatings on type 316 L stainless steel. Corros Sci 45:237–252
20. Indira K, Mudali UK, Nishimura T et al (2015) A review on TiO_2 nanotubes: influence of anodization parameters, formation mechanism, properties, corrosion behavior, and biomedical applications. J Bio Tribo Corros 1:28. doi:10.1007/s40735-015-0024-x
21. Oh SH, Finones RR, Daraio C et al (2005) Growth of nano-scale hydroxyapatite using chemically treated titanium oxide nanotubes. Biomater 26:4938–4943
22. Jonasova L, Muller FA, Helebrant A et al (2004) Biomimetic apatite formation on chemically treated titanium. Biomater 25:1187–1194
23. Kar A, Raja KS, Misra M (2006) Electrodeposition of hydroxyapatite onto nanotubular TiO_2 for implant applications. Surf Coat Tech 201:3723–3731
24. Indira K, Ningshen S, Mudali UK et al (2012) Effect of anodization parameters on the structural morphology of titanium in fluoride containing electrolytes. Mater Charact 71:58–65
25. Tamilselvi S, Raman V, Rajendran N (2006) Corrosion behavior of Ti–6Al–7Nb and Ti-6–Al–4V ELI alloys in simulated body fluid solution by electrochemical impedance spectroscopy. Electrochim Acta 52:839–846
26. Alves SA, Bayon R, Viteri VSD et al (2015) Tribocorrosion behavior of calcium- and phosphorous-enriched titanium oxide films and study of osteoblast interactions for dental implants. J Bio Tribo Corros 1:23. doi:10.1007/s40735-015-0023-y
27. Indira K, Mudali UK, Rajendran N (2014) In-vitro biocompatibility and corrosion resistance of strontium incorporated TiO_2 nanotube arrays for orthopaedic applications. J Biomater Appl 29:113–129
28. Deligianni DD, Katsala ND, Koutsoukos PG et al (2001) Effect of surface roughness of hydroxyapatite on human bone marrow cell adhesion, proliferation, differentiation and detachment strength. Biomater 22:87–96
29. Yoshinari M, Oda Y, Inoue T et al (2002) Bone response to calcium-phosphate coated and biphosphonate immobilized titanium implants. Biomater 23:2879–2885

30. Indira K, Mudali UK, Rajendran N (2014) In-vitro bioactivity and corrosion resistance of Zr incorporated TiO_2 nanotube arrays for orthopaedic applications. Appl Surf Sci 316:264–275

31. Lu MD, Yang SM (2009) Synthesis of poly(3-hexylthiophene) grafted TiO_2 nanotube composite. J Colloid Interf Sci 333:128–134

32. Nagarajan S, Rajendran N (2009) Surface characterization and electrochemical behavior of porous titanium dioxide coated 316L stainless steel for orthopaedic applications. Appl Surf Sci 255:3927–3932

33. Xin Y, Jiang J, Huo K et al (2009) Bioactive $SrTiO_3$ nanotube arrays: strontium delivery platform on Ti-based osteoporotic bone implants. ACS Nano 3:3228–3234

34. Liu X, Liu Z, Lu J et al (2014) Silver sulfide nanoparticles sensitized titanium oxide nanturbe arrays synthesized by in situ sulfurization for photocatalytic hydrogen production. J Colloid Interf Sci 413:17–23

35. Arunchandran C, Ramya S, George RP et al (2012) Corrosion inhibitor storage and release property of TiO_2 nanotube powder synthesized by rapid breakdown anodization method. Mater Res Bull 48:635–639

36. Sobieszczyk S (2009) Self-organized nanotubular oxide layer on Ti and Ti alloys. Adv Mater Sci 9:25–41

37. Okada M, Furuzono T (2011) Low temperature synthesis of nanoparticles-assembled, transparent, and low crystallized hydroxyapatite blocks. J Colloid Interf Sci 360:457–462

38. Koutsopoulos S (2002) Synthesis and characterization of hydroxyapatite crystals: a review study on the analytical methods. J Biomed Mater Res 62:600–612

39. Wei D, Zhou Y, Jia D et al (2008) Biomimetic apatite deposited on microarc oxidized anatase-based ceramic coating. Ceram Int 34:1139–1144

40. Tang H, Guo Y, Jia D et al (2010) High bone-like apatite-forming ability of mesoporous titania films. Micropor Mesopor Mater 131:366–372

41. Devi KB, Singh K, Rajendran N (2011) Sol–gel synthesis and characterisation of nanoporous zirconium titanate coated on 316L SS for biomedical applications. J Sol-Gel Sci Tech 59:513–520

42. Blazewicz M, Paluszkiewicz C (2001) Characterization of biomaterials used for bone regeneration by FTIR spectroscopy. J Mol Struct 563:147–152

43. Kasuga T, Kondo H, Nogami MJ (2002) Apatite formation on TiO_2 in simulated body fluid. J Cryst Growth 235:235–240

44. Kokubo T, Kushitani H, Sakka S et al (2004) Solutions able to reproduce in vivo surface-structure changes in bioactive glass-ceramic A-W3. J Biomed Mater Res 24:721–734

45. Amin MS, Randeniya LK, Bendavid A et al (2009) Amorphous carbonated apatite formation on diamond-like carbon containing titanium oxide. Diam Relat Mater 18:1139–1144

46. Sena LAD, Rocha NCC, Andrade MC et al (2003) Bioactivity assessment of titanium sheets electrochemically coated with thick oxide film. Surf Coat Tech 166:254–258

47. Song WH, Juna YK, Hana Y et al (2004) Bimimetic apatite coatings on micro-arc oxidized titania. Biomater 25:3341–3349

48. Kaciulis S, Mattogno G, Napoli A (1998) Surface analysis of biocompatible coatings on titanium. J Electron Spectrosc 95:61–69

49. Karthega M, Rajendran N (2010) Hydrogen peroxide treatment on Ti–6Al–4V alloy: a promising surface modification technique for orthopaedic application. Appl Surf Sci 256:2176–2183

50. Baszkiewicz J, Krupa D, Mizera J et al (2005) Corrosion resistance of the surface layers formed on titanium by plasma electrolytic oxidation and hydrothermal treatment. Vaccum 78:143–147

51. Saji VS, Choe HC, Brantley WA (2009) An electrochemical study of self-ordered nanoporous and nanotubular oxide on Ti–35Nb–5Ta–7Zr alloy for biomedical applications. Acta Biomater 5:2303–2310

52. Souza MEP, Ballester M, Freire CMA (2007) EIS characterization of Ti anodic oxide porous films formed using modulated potential. Surf Coat Tech 201:7775–7780

53. Raman V, Tamilselvi S, Nanjundan S et al (2005) Electrochemical behavior of titanium and titanium alloys in artificial saliva. Trends Biomater Artif Organs 18:137–140

54. Yu WQ, Qiu J, Zhang FQ (2011) In vitro corrosion study of different TiO_2 nanotube layers on titanium in solution with serum proteins. Colloids Surf B Biointerf 84:400–405

55. Yu WQ, Qiu J, Xu L et al (2009) Corrosion behaviors of TiO_2 nanotube layers on titanium in Hank's solution. Biomed Mater 4:065012

56. Tamilselvi S, Rajendran N (2007) In-vitro corrosion behavior of Ti–5Al–2Nb–1Ta alloy in Hank's solution. Mater Corros 58:285–289

57. Karthega M, Rajendran N (2011) Formation of a nanoporous oxide layer over a β—phase titanium in simulated body fluid. J Porous Mater. doi:10.1007/s10934-011-9507-4

58. Fekry AM, El-Sherif RM (2009) Electrochemical corrosion behavior of magnesium and titanium alloys in simulated body fluid. Electrochim Acta 54:7280–7285

59. Raman V, Tamilselvi S, Rajendran N (2007) Electrochemical impedance spectroscopic characterization of titanium during alkali treatment and apatite growth in simulated body fluid. Electrochim Acta 52:7418–7424

60. Wang CX, Wang M (2002) Electrochemical impedance spectroscopy study of the nucleation and growth of apatite on chemically treated pure titanium. Mater Lett 54:30–36